TD-DMRG Study of Exciton Dynamics with both Thermal and Static Disorders for Fenna-Matthews-Olson Complex

Published as part of Journal of Chemical Theory and Computation virtual special issue "First-Principles Simulations of Molecular Optoelectronic Materials: Elementary Excitations and Spatiotemporal Dynamics".

Zirui Sheng, Tong Jiang, Weitang Li,* and Zhigang Shuai*

ACCESS | Metrics & More | Article Recommendations | SI Supporting Information

ABSTRACT: Photosynthesis is a fundamental process that converts solar energy into chemical energy. Understanding the microscopic mechanisms of energy transfer in photosynthetic systems is crucial for the development of novel optoelectronic materials. Simulating these processes poses significant challenges due to the intricate interactions between electrons and phonons, compounded by static disorder. In this work, we present a numerically nearly exact study using the time-dependent density matrix renormalization group (TD-DMRG) method to simulate the quantum dynamics of the Fenna-Matthews-Olson (FMO) complex considering an eight-site model with both thermal and static disorders. We employ the thermo-field dynamics formalism for temperature effects. We merge all electronic interactions into one large matrix product state (MPS) site, boosting accuracy efficiently without increasing complexity. Previous combined experimental and computational studies indicated that the static disorders range from 30 to 90 cm^{-1} for different FMO sites. We employ a Gaussian distribution and the auxiliary bosonic operator approach to consider the static disorder in our TD-DMRG algorithm. We investigate the impact of different initial excitation sites, temperatures, and degrees of static disorder on the exciton dynamics and temporal coherence. It is found that under the influence of the experimentally determined static disorder strength, the exciton population evolution shows a non-negligible difference at zero temperature, while it is hardly affected at room temperature.
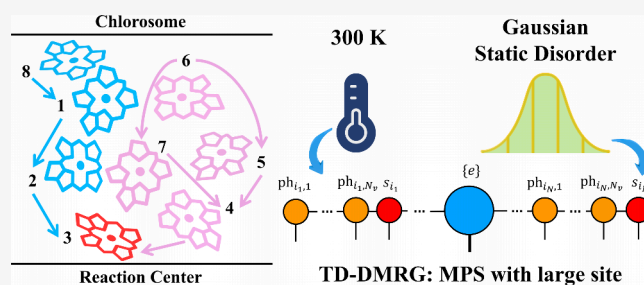
1. INTRODUCTION

Biomolecular systems for photosynthesis could be considered the earliest molecular materials that convert solar energy into biochemicals. The photosynthetic organisms have evolved a diverse range of light-harvesting complexes (LHCs) for photosynthesis,[1−3] which could be divided into three main processes: light-harvesting (LH), charge separation (CS), and biochemical reaction (BR).[4] During the LH process, light-harvesting antennas capture photons in the form of excitons which are delocalized over pigment molecules embedded in the protein environments of LHCs. Excitons generated in these LHCs maintain their delocalized nature and are effectively shielded from environmental perturbations. They traverse distances exceeding 100 nm in approximately 100 ps, arriving intact at the reaction center.[5] The small time scale of elementary excitations and spatiotemporal dynamics during the LH process has attracted widespread attention, and people have begun to study the origin of this high quantum efficiency of excitonic energy transport. The Fenna-Matthews-Olson (FMO) complex found in green sulfur bacteria is a prominent example of LHCs. FMO is a trimer pigment−protein complex (PPC) formed by three identical monomers, which serve as a

bridge linking the chlorosome to the reaction center. It stands out as one of the earliest LHCs whose structural data was obtained from X-ray crystallography,[6,7] leading to extensive spectroscopic and computational investigations. Later, people found that a wavelike energy transfer is an important reason for improving the efficiency of exciton dynamics. Whether the wavelike energy transfer within photosynthetic systems is an outcome of evolutionary complexity beyond synthetic replication is still unknown, but certain evidence such as coherent transfer observed in conjugated polymers or J-aggregates, hints at the potential for synthetic systems to exhibit similar energy transfer dynamics. However, none have been deliberately engineered for this specific mechanism. Designing systems optimized for wavelike energy transport necessitates precise control over chromophore spatial positions
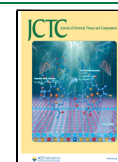
and orientations, dictating electronic couplings and the spectral bath of surrounding phonon modes. The applications of such materials could span optoelectronics, solar light harvesting, on-pixel processing, and excitonic devices.[8]

Initially, it was believed that each monomer of FMO contained seven well-established bacteriochlorophyll-a (BChl) pigment molecules. However, subsequent confirmation of an eighth BChl may prompt a reevaluation of the energy-transfer process within the FMO complex.[9−11] In the earlier days, it was believed that both Bchl 1 and Bchl 6 might be two possible starting points for exciton transport because of similar distance from the antenna complex, and respectively lead to two paths of energy transfer: $1 \rightarrow 2 \rightarrow 3$ (path A) and $6 \rightarrow (5, 7) \rightarrow 4 \rightarrow 3$ (path B).[12−14] But due to the special position that the eighth chromophore resides roughly midway between the baseplate and the Bchl 1,[10] this eighth Bchl may serve as the primary acceptor of excitation energy from the chlorosome and provides a route preference to path A.[11,15] A sketch about the two energy transfer paths in the eight-site FMO model are shown in Figure 1.
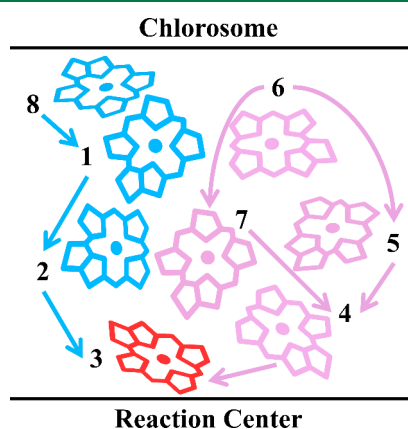

Figure 1. Schematic diagram of the eight-site FMO model. The blue arrows represent the energy transfer path A: $8 \rightarrow 1 \rightarrow 2 \rightarrow 3$, and the pink arrows represent path B: $6 \rightarrow (5, 7) \rightarrow 4 \rightarrow 3$. Site 8 links the chlorosome (baseplate), and site 3 links the reaction center complex.

The analysis of the energy-transfer characteristics of an eight-site FMO model incorporated considerations of thermal motion utilizing the generalized Bloch-Redfield method,[16] but the static disorder of the electronic degrees of freedom (DoFs) was neglected. Static disorder is a kind of disorder that presents as a change in the local excitation energy, corresponding to the change of the diagonal elements of transfer integral. This deviation of site energies can stem from various sources, including static defects such as lattice imperfections (like stacking faults, dislocations, grain boundaries, and impurities), as well as phonons characterized by frequencies significantly lower than the exciton bandwidth.[17,18] For aggregates like FMO, they are usually embedded in a polymer matrix or a protein scaffold which produces static disorder.[19]

Since P. Anderson proposed the Anderson localization theory,[20] people started to study the features that disorder introduced into charge transport.[21−24] An important reason for the widespread interest in the FMO complex is that through two-dimensional electronic spectroscopy (2DES), researchers found oscillations of small amplitude, which were called quantum beats (QBs) and regarded as the signal of coherences. The debate over whether these coherences are vibrational or

interexciton in nature[25−28] has stimulated a lively discussion in the field of quantum biology.[29,30] Unlike highly ordered crystals, the pigments within biological systems are enveloped in a warm, wet, and disordered environment, where the coupling strength between pigments is often comparable to the interaction with the surrounding environment. The system-bath coupling combined with static disorder tends to confine the excitation to a limited number of pigments even in highly coupled antenna complexes.[31,32] Static disorder, present in FMO, leads to inhomogeneous optical dephasing in 2DES experiments, where researchers capture a snapshot of the collective behavior during ultrafast measurements.[33] A closer consideration of static disorder shows great importance for clearer observation of quantum beats and a better understanding of coherence dynamics. Early studies employed time-averaging site energies in quantum mechanics/molecular mechanics simulations to evaluate the site energy fluctuation. However, discrepancies arise due to differing potential energy surfaces in classical and quantum descriptions of the pigments.[34−40] Various strategies have been proposed to mitigate this geometry mismatch issue, though many are computationally intensive.[41−43] A cost-effective approach involves leveraging the floppy inclusions and rigid substructure topography (FIRST) alongside the framework-rigidity-optimized dynamic algorithm (FRODA) methods,[44] which was combined with the charge density coupling (CDC) method[45] to conduct a quantum chemical/electrostatic analysis of static disorder, highlights electrostatics as the primary contributor to static disorder in site energies according to the alignment between calculated optical spectra for the heterogeneous ensemble and experimental data, and provides the static disorder values on each monomer of FMO and the analysis of the coherence of static disorder.[46] Efficient energy transfer in the FMO complex persists in the presence of static disorder, emphasizing the importance of comprehending the mechanisms of energy transport amid such disorder. This understanding is crucial for gaining deeper insights into coherent transport within FMO and other photosynthetic systems; and also, while driving progress in designing and developing innovative materials customized for efficient energy transfer,[47] an in-depth understanding of the mechanism of exciton localization caused by static disorder in biological systems is also valuable for other abiotic disorder systems.[48,49]

The time-dependent density matrix renormalization group (TD-DMRG) and its response algorithms have been developed as a powerful toolbox for studying the spectroscopy,[50−52,52,53] quantum diffusion dynamics,[54−59] electrical and thermal transport[60,61] of optoelectronic systems including biomolecules, molecular crystals and junctions. This toolbox utilizes the matrix product states (MPS) to decompose the many-body wave function into matrices, allowing for systematic improvement of accuracy by increasing the size of these matrices, controlled by the bond dimension. The accuracy achieved by TD-DMRG is comparable to the gold standard for quantum dynamics, the multiconfiguration time-dependent Hatree method (MCTDH)[62,63] and its multilayer (ML) extension,[64] offering a more flexible and simple algorithmic framework. By employing the time-dependent variational principle,[65] TD-DMRG efficiently simulates the time-dependent behavior of quantum electron-vibrational systems with hundreds to thousands of degrees of freedom.[56] Previous studies employing TD-DMRG have explored exciton dynamics within the FMO complex, focusing exclusively on a 7-site

model and omitting the influence of static disorder.[66−68] Similarly, the ML-MCDTH approach has been applied without accounting for static disorders.[69] Incorporating static disorder into TD-DMRG simulations is challenging, requiring averaging over numerous independent TD-DMRG runs (thousands or more) with site energy sampling. An effective boson mode can be derived to form an effective Hamiltonian which accounts for the effect of static disorder,[70] eliminating the need for extensive sampling and obtaining static disorder influenced result with only one shot TD-DMRG calculation.

In this study, we incorporate the static disorder effect by adding the auxiliary mode into TD-DMRG calculation, which allows the numerically accurate full quantum study of the exciton dynamics with the impact of the static disorder at finite temperature, and we apply the approach to the FMO complex. The rest of the paper is structured as follows. In Section 2 we introduce the model used to describe the excition-phonon coupling and give out the approach that uses thermo-field TD-DMRG with auxiliary bosonic operators to simultaneously address temperature effect[71] and static disorder.[70] Also, we introduce different MPS configurations, including the large site MPS configuration. In Section 3 we find out the most efficient and accurate configuration, which is employed to perform all the calculations. We study the specific impact of the eighth site and the temperature effect on exciton dynamics. Furthermore, we assess the effects of varying magnitudes of static disorder on energy transfer, considering both model parameters and realistic excitation energy distributions obtained from existing literature.[46] Through the analysis, we not only focus on the exciton population but also the coherence between different sites. We conclude the paper and outline future research prospects in Section 4.

2. THEORY

2.1. Exciton-Vibrational Hamiltonian with Disorder.
This section introduces the exciton-vibrational Hamiltonian for FMO complexes along with the Hamiltonian that includes an auxiliary bosonic degree of freedom to account for the impact of static disorder. Exciton-vibrational models are widely used to model molecular aggregates and molecular materials,[17,72] with the diabatic potential energy surfaces represented by polynomials of nuclear coordinates.[73] For the FMO aggregates, the system dynamics can be demonstrated by a classical exciton-vibrational model called the Frenkel-Holstein model, containing vibrational modes with different frequencies coupled to excited electronic states. For a lattice consisting of N sites (site index i), the Frenkel-Holstein Hamiltonian containing static disorder can be written in terms of J_{ij}, g_{ik}, and ω_{ik} as follows:

$$\hat{H}_{FH} = \sum_{i,j}^{N} J_{ij}a_i^\dagger a_j + \sum_{i}^{N}\sum_{k}^{N_v} \omega_{ik}b_{ik}^\dagger b_{ik}$$
$$+ \sum_{i}^{N}\sum_{k}^{N_v} g_{ik}\omega_{ik}(b_{ik}^\dagger + b_{ik})a_i^\dagger a_i \tag{1}$$

Here $a_i^\dagger$ (a_i) are the raising (lowering) operator for local excited state $|i\rangle$, J_{ij} are the electronic excitation energies ($i = j$) and couplings come from Coulomb interactions ($i \neq j$), $b_{ik}^\dagger$ (b_{ik}) are the creation (annihilation) operators of the kth harmonic mode of exciton state $|i\rangle$ with frequency ω_{ik}, g_{ik} are the electron-vibrational coupling parameters.

The parameters J_{ij} comes from the Frenkel exciton eight-site FMO Hamiltonian reported in ref 16, shown in eq 2 with unit of cm^{-1}, and in this work, all the frequencies of harmonic modes are got by discretizing the original spectral density into 74 modes[69] in total within the interval ranging from 2 to 300 cm^{-1}.

$$
J = \begin{pmatrix}
310 & -98 & 6 & -6 & 7 & -12 & -10 & 38 \\
-98 & 230 & 30 & 7 & 2 & 12 & 5 & 8 \\
6 & 30 & 0 & -59 & -2 & -10 & 5 & 2 \\
-6 & 7 & -59 & 180 & -65 & -17 & -65 & -2 \\
7 & 2 & -2 & -65 & 405 & 89 & -6 & 5 \\
-12 & 11 & -10 & -17 & 89 & 320 & 32 & -10 \\
-10 & 5 & 5 & -64 & -6 & 32 & 270 & -11 \\
38 & 8 & 2 & -2 & 5 & -10 & -11 & 505
\end{pmatrix}
\tag{2}
$$

The static disorder usually comes from the environment, solvation, etc., and finally renders as the shift of local site excitation energy (the diagonal elements of J matrix). The deviations in site energies are usually modeled as random Gaussian variables, where the width of their distribution, denoted as s, escalates with increasing temperature.[17] In FMO complex, calculations on optical spectra with experimental data indicate that electrostatics is the dominant contributor to static disorder in site energies.[46] A typical way to account for this influence on the site energies is by adding disorder with Gaussian distribution to the diagonal terms in eq 2 and averaging the results over the independent calculations based on the perturbed Hamiltonians. If a variable x satisfies Gaussian distribution, then the probability distribution can be written as $P_x = \frac{1}{s\sqrt{2\pi}}e^{-(x-\mu)^2/2s^2}$, where s is the standard deviation, μ is the expectation. We use Ω_{il} to represent static disorder variables and assume P_{Ω_i} is a standard Gaussian distribution, then $s_{il}\Omega_{il}$ will satisfy a Gaussian distribution with standard deviation s_{il}. Hence we can use s_{il} as a parameter to quantify the size of static disorder corresponding to Ω_{il}, which determines the amplitude of the distribution.

An auxiliary bosonic mode can be introduced into the original Hamiltonian in eq 1,

$$\hat{H}_{FH-S} = \sum_{i,j}^{N} J_{ij}a_i^\dagger a_j + \sum_{i}^{N}\sum_{k}^{N_v} \omega_{ik}b_{ik}^\dagger b_{ik}$$
$$+ \sum_{i}^{N}\sum_{k}^{N_v} g_{ik}\omega_{ik}(b_{ik}^\dagger + b_{ik})a_i^\dagger a_i$$
$$+ \sum_{i}^{N}\sum_{l}^{N_d} V_{il}\frac{s_{il}}{\sqrt{2}}(z_{il}^\dagger + z_{il})a_i^\dagger a_i \tag{3}$$

where the distribution functions of the probability density of static disorder are set to satisfy the Gaussian function form $P_{\Omega_i} = \prod_l \frac{1}{\sqrt{2\pi}}e^{-\Omega_{il}^2/2}$, and the stochastic static disorder variables can be treated as harmonic oscillator coordinates similar to the vibrational part $\Omega_{il} = \frac{(z_{il}^\dagger + z_{il})}{\sqrt{2}}$, which was proposed by Borrelli and Gelin.[70] V_{il} specifies the coupling of it to the electronic subsystem. N_v and N_d are the number of parameters of phonons and static disorders, respectively. In this work, we assume there is only one static disorder DoF

within every site, and each static disorder only takes effect on the site they are in, then we have $N_d = 1$.

2.2. Finite Temperature Formalism with Thermo-field Dynamics.
The temperature effect is not negligible in biomolecular aggregates like FMO because the vibration frequency, exciton coupling, and energy scale of the organic molecules are in a similar magnitude, which means that the influence of temperature on the excited physical processes of the molecular aggregates is not negligible. A thermodynamic system at a finite temperature is a statistical ensemble known as a mixed state, which cannot be described by a wave function. The phonon part could be treated as a canonical ensemble, the density matrix and partition function is

$$\hat{\rho} = \frac{e^{-\beta \hat{H}}}{Z_{ph}}, \quad Z_{ph}(\beta) = \sum_{\{n_k\}}' e^{-\beta \sum_k n_k \omega_k} = \sum_{n_1 n_2 \dots} \prod_k e^{-\beta n_k \omega_k}$$
$$= \prod_k \sum_{n_k} e^{-\beta n_k \omega_k} \tag{4}$$

$\sum'$ represents the sum of all occupation numbers that satisfy the constraint on the total number of particles $\{n_1, n_2, \dots\}$, $n_k \in \{0, 1, 2, \dots\}$. The density matrix represents the distribution of particles in different energy states and it is a function of temperature. Therefore, the temperature will affect the thermal equilibrium distribution of phonons in energy space and then affect the system-bath dynamics. Thermo-field dynamics (TFD) is a method that enabled us to include the temperature parameter in a special mathematical transformation,[74−77] and the TFD method combined with matrix product states approach was first proposed by Borrelli and Gelin.[71] We introduce the TFD formalism for the simulation of time-dependent exciton dynamics at finite temperature as follows.[70]

The system and bath are assumed to be decoupled at the beginning and only the bath DoFs are in the thermal equilibrium. In most system-bath model problems, to get a pure state, for a mixed state with a temperature of T in the physical space P, the auxiliary space $\tilde{P}$ needs to be introduced. But in the FMO dynamics, the initial system is a pure state, so we only introduce the auxiliary space $\tilde{P}$ of the phonon part. The pure state wave function at zero time can be written as

$$|\Psi(0)\rangle = |\Psi_e\rangle \otimes |\Psi_{ph}\rangle = |e\rangle \otimes |\Psi_{ph}\rangle \tag{5}$$

The Hamiltonian in the extended space is $\hat{H}_{P\tilde{P}} = \hat{H}_P - \hat{H}_{\tilde{P}}$, then the wave function obeys

$$i\frac{\partial}{\partial t}|\Psi(t)\rangle = \hat{H}_{P\tilde{P}}|\Psi(t)\rangle \tag{6}$$

Suppose the Hamiltonian corresponding to the vibrational part of P space is $\hat{H}_{P,ph} = \sum_k \omega_k b_k^\dagger b_k$, then the vibrational part wave function is

$$|\Psi_{ph}\rangle = \prod_k \sum_n \frac{e^{-\beta \hat{H}_{P,ph}/2}}{\sqrt{Z_{ph}(\beta)}}|n_k, \tilde{n}_k\rangle$$
$$= \prod_k \sum_n \frac{e^{-\beta \omega_k b_k^\dagger b_k/2}}{\sqrt{Z_{ph}(\beta)}}|n_k, \tilde{n}_k\rangle \tag{7}$$

where $|n_k, \tilde{n}_k\rangle = |n_k\rangle|\tilde{n}_k\rangle$, $|n_k\rangle$ are the eigenvectors of the kth harmonic mode, $|\tilde{n}_k\rangle$ is the copy of $|n_k\rangle$ in the tilde space. Define the collective vacuum state for both physical and auxiliary vibrational DoFs: $|0_k, \tilde{0}_k\rangle = \sum_n \frac{e^{-\beta \omega_k b_k^\dagger b_k/2}}{\sqrt{Z_{ph}(\beta)}}|n_k, \tilde{n}_k\rangle$.

There is an entanglement between the patterns in each physical space and their one-to-one counterparts in the auxiliary space. Then the Bogoliubov transformation was introduced, which could fully remove this entanglement:

$$|\Psi_{ph}\rangle = e^{iG} \prod_k |0_k, \tilde{0}_k\rangle \tag{8}$$

$$G = -i \sum_k \theta_k(b_k^\dagger \tilde{b}_k^\dagger - b_k \tilde{b}_k), \quad \theta_k = \text{arctanh}(e^{-\beta \omega_k/2}) \tag{9}$$

By defining $|\phi(t)\rangle = e^{-iG}|\Psi(t)\rangle$, the Schrödinger equation can be written as

$$i\frac{\partial}{\partial t}|\phi(t)\rangle = e^{-iG}\hat{H}_{P\tilde{P}}e^{iG}|\phi(t)\rangle \tag{10}$$

Therefore, when simulating the exciton diffusion behavior in FMO, the excited state can be prepared directly in the electron part as the initial state of evolution:

$$|\phi(0)\rangle = |e\rangle \prod_k |0_k, \tilde{0}_k\rangle \tag{11}$$

then the dynamic evolution problem of finite temperature is transformed into a problem that uses an effective Hamiltonian $\bar{H} = e^{-iG}\hat{H}_{P\tilde{P}}e^{iG}$ to directly do the real-time evolution with a known initial wave function. Temperature effects are included in this transformation.

Based on the above calculations, the transformed Frenkel-Holstein Hamiltonian containing static disorder could be obtained:

$$\bar{H} = e^{-iG}\left(\hat{H}_P - \sum_{ik} \omega_{ik}\tilde{b}_{ik}^\dagger \tilde{b}_{ik}\right)e^{iG} = \sum_{i,j}^N J_{ij}a_i^\dagger a_j$$
$$+ \sum_i^N \sum_k^{N_v} \omega_{ik}(b_{ik}^\dagger b_{ik} - \tilde{b}_{ik}^\dagger \tilde{b}_{ik})$$
$$+ \sum_i^N \sum_k^{N_v} g_{ik}\omega_{ik}[\cosh(\theta_{ik})(b_{ik}^\dagger + b_{ik}) + \sinh(\theta_{ik})(\tilde{b}_{ik}^\dagger + \tilde{b}_{ik})]a_i^\dagger a_i$$
$$+ \sum_i^N \sum_l^{N_d} V_{il}\frac{s_{il}}{\sqrt{2}}(z_{il}^\dagger + z_{il})a_i^\dagger a_i \tag{12}$$

where $\hat{H}_P = \hat{H}_{FH-S}$. Moreover, we can get the expectation of an arbitrary operator $\hat{A}$:

$$\langle \hat{A}(t)\rangle = \langle 0_d|\langle e, \Psi_{ph}|e^{i(\hat{H}_P - \hat{H}_{\tilde{P}})t}\hat{A}e^{-i(\hat{H}_P - \hat{H}_{\tilde{P}})t}|\Psi_{ph}, e\rangle|0_d\rangle$$
$$= \langle 0_d|\langle 0_v\tilde{0}_v|\langle e|e^{i\bar{H}t}\hat{A}e^{-i\bar{H}t}|e\rangle|0_v\tilde{0}_v\rangle|0_d\rangle \tag{13}$$

where $|0_v\tilde{0}_v\rangle = \prod_{i,k}|0_{ik}, \tilde{0}_{ik}\rangle$, $|0_d\rangle = \prod_{i,l}\frac{1}{\sqrt[4]{2\pi}}e^{-\Omega_{il}^2/4}$. Then the time propagation can be performed using extremely efficient methods based on the MPS formalism, leading to enormous computational savings in the calculation of expectation values of operators averaged over static disorder. Utilizing the finite-temperature representation of the Schrödinger equation, a computationally efficient and numerically exact wave function-based approach, as will be introduced in Sec. 2.3, has been developed for assessing quantum observables averaged over static disorder, denoted as $\hat{A}(t)$ above. This method incorporates static-disorder variables into the system Hamiltonian, treating them as harmonic modes that influence the

electronic parameters of the system.[70] When considering the numbers of electronic, vibrational, and static-disorder DoFs in the system as N_e, N_v, and N_d respectively, the methodology introduced in this research only requires a single propagation of the system's wave function with N_e electronic and $2N_v + N_d$ vibrational DoFs. The total formalism proposed by Borrelli and Gelin offers large substantial computational efficiencies.

2.3. TD-DMRG. The modern DMRG employs the MPS and matrix product operator (MPO) to represent wave function and operator.[78,79] An arbitrary n-dimensional many-body wave function can be decomposed by singular value decomposition (SVD). While doing SVD operation $C = USV^\dagger$, we get three matrices, where the dimension of matrix U is $N_A \times N_C$, the dimension of S is $N_C \times N_C$, and the dimension of $V^\dagger$ is $N_C \times N_B$, $N_C = \min(N_A, N_B)$. S is diagonal, and the diagonal elements are called the singular values. Through SVD, the many-body wave function can be decomposed like this:

$$|\Psi\rangle = \sum_{\{\sigma\}} C_{\sigma_1, \sigma_2 \dots \sigma_n} |\sigma_1, \sigma_2 \dots \sigma_n\rangle$$
$$= \sum_{\{\sigma\}, a_1} U_{\sigma_1, a_1} S_{a_1, a_1} V^\dagger_{a_1, \sigma_2 \dots \sigma_n} |\sigma_1, \sigma_2 \dots \sigma_n\rangle = \cdots \tag{14}$$

which can be finally transformed into the form of MPS by a sequence of SVD operations,

$$|\Psi\rangle = \sum_{\{\sigma\}, \{a\}} A^{\sigma_1}_{a_1} A^{\sigma_2}_{a_1 a_2} \dots A^{\sigma_n}_{a_{n-1}} |\sigma_1, \sigma_2 \dots \sigma_n\rangle \tag{15}$$

This process of obtaining MPS from the wave function through SVD can be described using the graph of tensor networks, which is shown in Figure 2. It can be seen from the
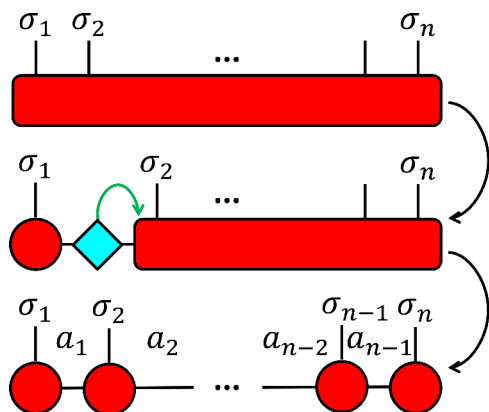

Figure 2. A diagram of converting the wave function into MPS through SVD in tensor network form.

graph that $A^{\sigma_l}_{a_{l-1}, a_l}$ is a three-dimensional tensor. Generally, the bonds $|\sigma_i\rangle$ facing upward are called physical bonds, and the bonds $|a_i\rangle$ connecting different matrix lattices are called virtual bonds. DMRG uniquely controls the accuracy of the calculation by setting the maximum virtual bond dimension M, then only the biggest M singular values will be reserved through SVD. The number of parameters in the MPS wave function is polynomial ($\sim O(pM^2n)$). In Figure 2 the SVD process is done from left to right, which can also be done from right to left or from both sides to the middle, giving different canonical forms of MPS. The canonical center matrix is moved during the processes of ground state calculation and time-dependent propagations.

Similarly, the MPO form of a general operator $\hat{O}$ can be written as

$$\hat{O} = \sum_{\{w\},\{\sigma\},\{\sigma'\}} W^{\sigma_1',\sigma_1}_{w_1} W^{\sigma_2',\sigma_2}_{w_1 w_2} \cdots W^{\sigma_n',\sigma_n}_{w_{n-1}} |\sigma_1'\sigma_2'\cdots\sigma_n'\rangle\langle\sigma_n\sigma_{n-1}\cdots\sigma_1| \tag{16}$$

and the tensor network graph of MPO is shown in Figure 3, in order to distinguish between MPS and MPO, we use circle for MPS sites and square for MPO sites. Each MPO site has two physical bonds.
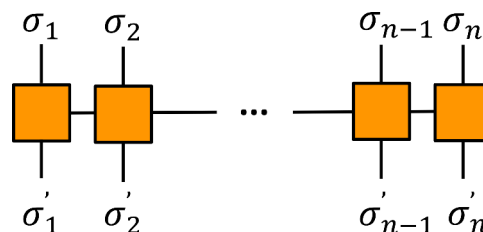

Figure 3. A tensor network graph of MPO.

According to eq 15 and eq 16, the MPS and MPO are expressed in the site basis $\{\sigma_1, \sigma_2, \dots \sigma_n\}$, the order of which affects the performance of DMRG in terms of accuracy, convergence, etc. Another operation of grouping clusters of related orbitals into large sites[80,81] shows potential for higher efficiency of calculation. So two kinds of TD-DMRG configurations with different electronic basis and site orderings are considered, which are shown in Figure 4. Assume the arrangement of electronic sites is ordered as $\{i_1, i_2, \dots, i_N\}$, N is the number of electronic sites, and each electronic site can be represented as e_{i_j}. Then if Config 1 in Figure 4(a) is considered, all vibrational sites $\mathrm{ph}_{i_j,k}$ are set to the right place of e_{i_j} and ordered according to k from 1 to N_v, where N_v is the total amount of vibrational modes. Each static disorder site s_{i_j} is placed after vibrational sites with the same i_j index. While Config 1 is a more commonly used configuration, another arrangement of MPS sites including a clustered large site was also taken into account. In Figure 4(b), Config 2 shows the same ordering of phonon sites and static disorder sites as Config 1, but all the electronic DoFs are grouped into one large site and placed in the center of the rest sites. In Sec. 3 these two configurations will be compared and the better arrangement will be selected for subsequent calculations.

We perform TD-DMRG calculation with the time dependent variational principle (TDVP) evolution scheme, which has been recognized as the most efficient one among many schemes.[50,68,78,83] An evolutionary scheme rooted in the TDVP known as projector-splitting (PS) is used. TDVP-PS has demonstrated a remarkable balance between accuracy and computational efficiency,[68] prompting its selection as the methodology of choice for our research endeavors. The Dirac-Frenkel TDVP is[84,85]

$$\langle\delta\Psi(t)_M | i\frac{\partial}{\partial t} - \hat{H} | \Psi(t)_M\rangle = 0 \tag{17}$$

Geometrically, this variational process is to project the time derivative of the wave function $-i\hat{H}|\Psi(t)_M\rangle$ into the MPS manifold $\mathcal{M}_{\mathrm{MPS}}$ in which $|\Psi(t)_M\rangle$ is located. The MPS manifold here refers to the space that MPS can take in all cases
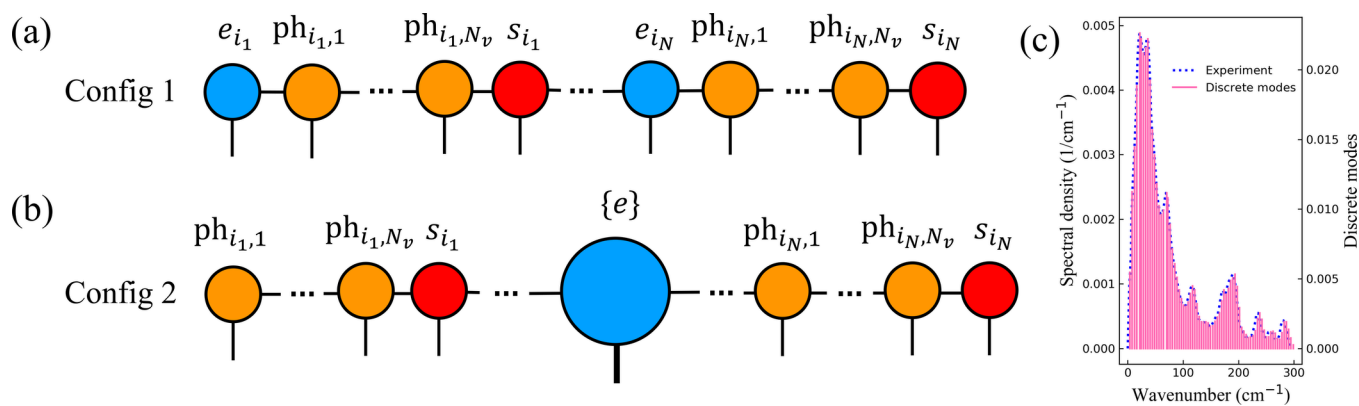
Figure 4. Two kinds of MPS configurations and the 74 vibrational modes used in the model. In (a) and (b): The blue site marked with e_{i_j} represents the electronic site at position $i_j \in \{i_1, i_2, ..., i_N\}$, N is the amount of electronic sites, while $\{i_1, i_2, ..., i_N\}$ is the arrangement of electronic sites. The orange site marked with $ph_{i_j,k}$ represents the vibrational site corresponding to e_{i_j}, $k \in \{1, 2, ..., N_v\}$, N_v is the amount of phonon modes. The red site marked with s_{i_j} represents the static disorder site corresponding to e_{i_j}. In Config 1, $ph_{i_j,k}$ are arranged to the right of e_{i_j} according to k from 1 to N_v, s_{i_j} is placed to the right of $ph_{i_j,k}$. In Config 2, all phonon sites and static disorder sites in Config 1 are maintained in place, all electronic sites are extracted and clustered into a large site, then inserted into the center of rest sites. (c) Experimental spectral density for FMO complex of *Pc. aestuarii*[82] (dotted) and approximate stick spectrum(solid rods).

when the dimensionality of the virtual key is fixed. $|\Psi(t)_M\rangle$ represents the MPS with the virtual bond dimension M,

$$\frac{\partial \Psi(t)_M}{\partial t} = -i\hat{P}_{\mathcal{M}_{MPS}}\hat{H}|\Psi(t)_M\rangle \tag{18}$$

The projection operator is

$$\hat{P}_{\mathcal{M}_{MPS}} = \sum_{i=1}^{N} \hat{P}[1: i-1] \otimes \hat{I}_i \otimes \hat{P}[i+1: N]$$
$$- \sum_{i=1}^{N-1} \hat{P}[1: i] \otimes \hat{P}[i+1: N] \tag{19}$$

where

$$\hat{P}[1: i] = \sum_{a_i, a_i'} |a_i'[1{:}i]\rangle S[1: i]_{a_i'a_i}^{-1} \langle a_i[1: i]| \tag{20}$$

$$\hat{P}[i+1: N] = \sum_{a_i, a_i'} |a_i'[i+1: N]\rangle S[i+1: N]_{a_i'a_i}^{-1}$$
$$\langle a_i[i+1: N]| \tag{21}$$

$$\hat{I}_i = \sum_{\sigma_i} |\sigma_i\rangle\langle\sigma_i| \tag{22}$$

$$\hat{P}[1: 0] = \hat{P}[N+1: N] = 1 \tag{23}$$

here

$$|a_i[1: i]\rangle = \sum_{\{a\},\{\sigma\}} A_{a_1}^{\sigma_1} A_{a_1 a_2}^{\sigma_2} \cdots A_{a_{i-1}a_i}^{\sigma_i} |\sigma_1 \cdots \sigma_i\rangle \tag{24}$$

$$S[1: i]_{a_i a_i'} = \langle a_i[1: i]|a_i'[1: i]\rangle \tag{25}$$

This method stems from the observation that the tangent space projector, as outlined in eq 17, remains invariant across various gauge conditions.

3. RESULTS AND DISCUSSION

3.1. The Ordering and Large Site MPS. The performance of MPS related method favors low entanglement between the DoFs when applied to both *ab initio* and electron−phonon systems,[86−89] owning to its one-dimensional structure, as shown in Figure 4. Prior to studying the exciton dynamics in FMO, we compare the performance with different ordering of the DoFs in eq 13. In accordance with the guidelines outlined in Sec. 2.3, two kinds of MPS configurations were computed. We employ an empirical approach to order the DoFs in the MPS chain for Config 1. Specifically, we position electronic sites of Bchl 8 and 1 at the center, which are identified as the potential excitation sites that will studied later, with the remaining sites positioned symmetrically on either side: [7, 5, 3, 1, 8, 2, 4, 6].[68] In the Config 1 setup, each electronic site is followed with its corresponding phonon sites and arranged following the aforementioned order, with all phonon modes obtained through a discretization method generating a total of 74 distinct vibrations from experimental values,[56,69,82] which is shown in Figure 4(c). There have been many studies focusing on the exciton dynamics in FMO,[16,19,69,90,91] but finite-temperature calculations involving such a large number of vibrational modes and taking into account static disorder are scarce. Notably, due to the unique characteristics of the TFD method, an auxiliary space phonon mode is associated with each physical space phonon mode, resulting in a total of 148 phonon sites corresponding to an electron site. The phonon sites linked to each electron site were organized in ascending order, as we did in the previous works.[50,68] In Sec. 3.3 the static disorder will be considered, so there will also be static disorder sites, each static disorder site is placed on the right side of all phonon sites corresponding to the same electron site. On the other hand, in Config 2, the phonon sites were positioned the same as in Config 1, and all electron sites were combined into one large site and placed in the middle of all phonon sites. We calculate the exciton evolution considering two initially excited sites, the excitation pattern is chosen to be Franck−Condon excitation (details see Supporting Information). Subsequently, the outcomes of both MPS configurations with varying
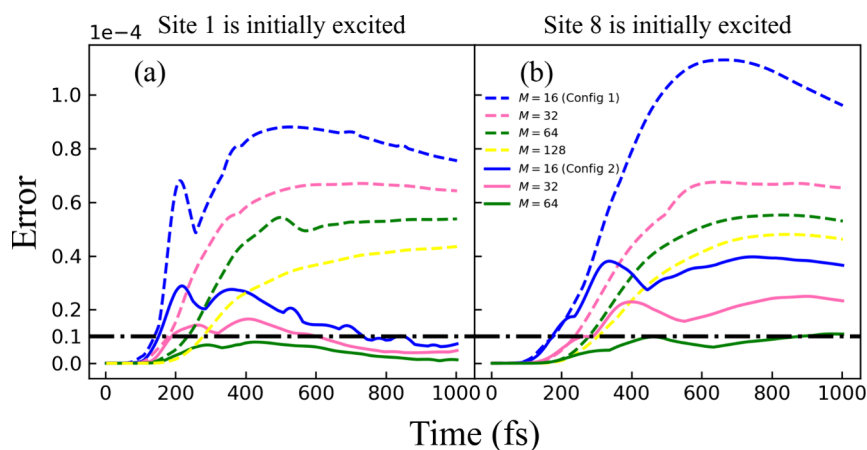
Figure 5. Mean cumulative deviation as a function of evolution time t for different MPS configurations, different maximum bond dimension M with the result of Config 2 MPS ($M = 128$) to $t = 1000$ fs when site 1 (a) or 8 (b) is initially excited. The deviations of Config 1 and Config 2 are shown by dashed and solid lines, respectively. The temperature is 300 K.
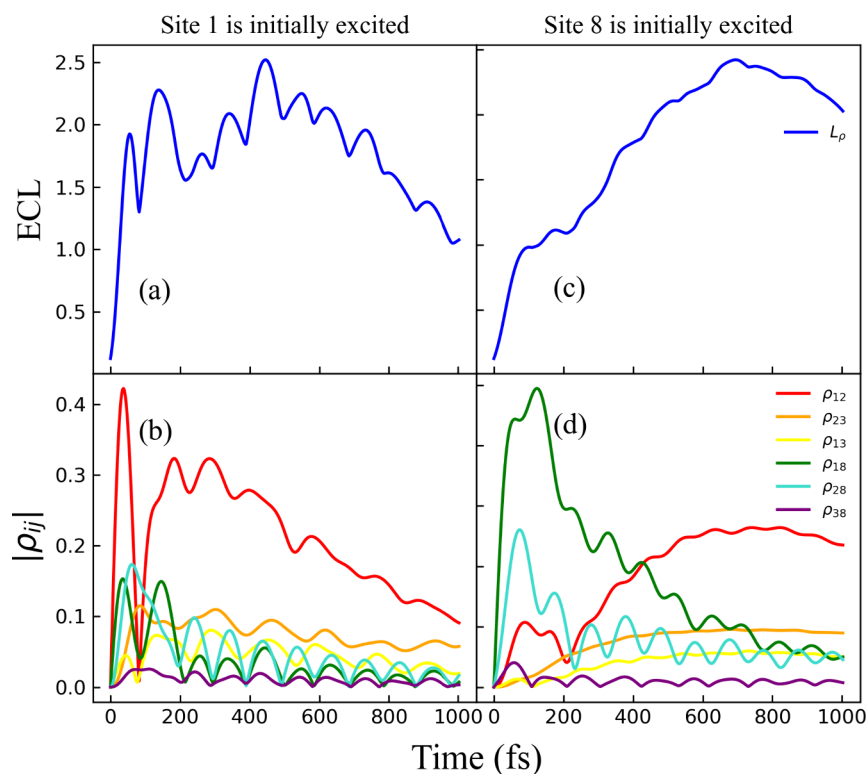

Figure 6. Time evolution of total ECL (a and c) and the coherence between different sites (b and d) in the eight-site model of FMO calculated with TD-DMRG when site 1 (a and b) or 8 (c and d) is initially excited. The temperature is 0 K.

maximum physical bond dimensions were critically analyzed, gauging the error of each result against the reference value obtained from Config 2 when $M = 128$. The mean cumulative deviation of exciton populations at time t is taken to be the error to quantitatively evaluate the relative accuracy in our calculations,

$$\text{Error}(t) = \frac{\sum_{i=1}^{8} \int_0^t |P^{(i)}(t') - P_{\text{ref}}^{(i)}(t')| dt'}{8t} \tag{26}$$

here $P^{(i)}$ represents the exciton population at the ith site of the eight-site FMO model. Analysis of the results depicted in Figure 5 revealed a diminishing error trend for Config 2 of MPS with increasing M, contrasting the consistently higher

error rates exhibited by Config 1 at the same M. Noteworthy is the observation that as M increased, the error associated with the normal MPS configuration gradually diminished, indicative of an approaching convergence between the results of Config 1 and Config 2. The intrinsic capabilities of MPS algorithms manifest in the likelihood of obtaining consistent results with larger M values, underscoring the superior accuracy achieved by Config 2. Another point is that the error of $M = 64$ is mostly less than 10^{-5} during 1000 fs while either site 1 or 8 as the excitation starting point, which shows the good convergence of Config 2, indicating that $M = 128$ has been able to obtain results precisely. It could be proved that Config 1 also behaves well for the convergence when M gradually increases, which are shown in Figure S3. Consequently, the Config 2 setup was
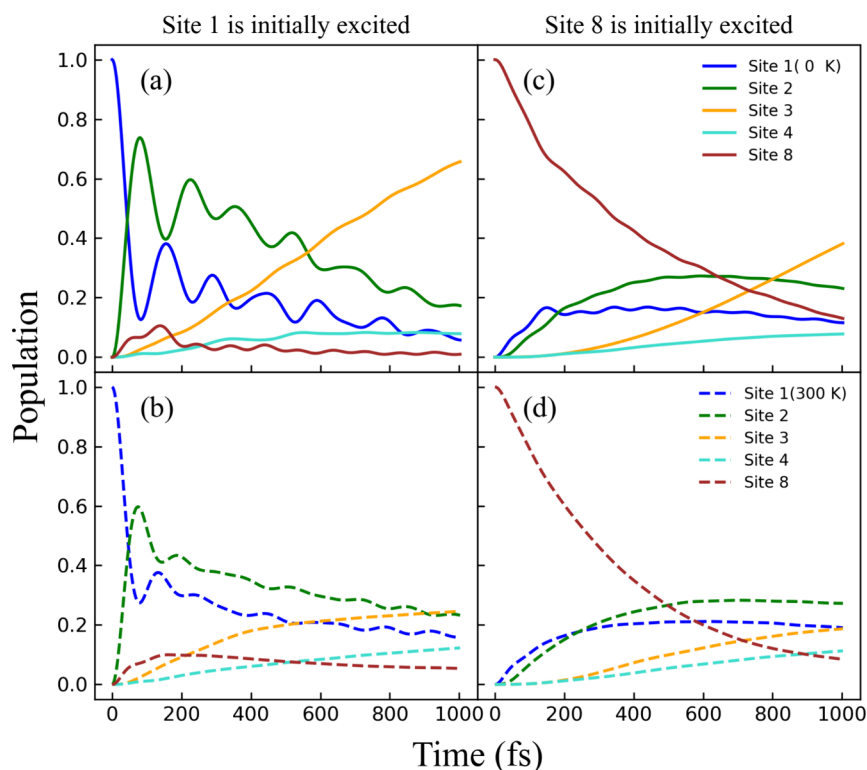
Figure 7. Site populations in the eight-site model of FMO calculated with the TD-DMRG when Bchl 1 (a, b) or 8 (c, d) is initially excited. In (a) and (c), the temperature is 0 K, while in (b) and (d) it is 300 K. The populations of the remaining sites 5, 6, and 7 are never larger than 10% and not shown. In all cases, the maximum bond dimension is $M = 128$.

selected for subsequent calculations based on its demonstrated precision and reliability in comparison to Config 1.

3.2. Eight-Site Model with Thermal Effects. Next, we analyze the energy transfer processes within the eight-site model of the FMO complex. Initially, we study the evolution of exciton coherence properties within the system over time. Exciton coherence length (ECL) serves as a crucial metric for quantifying the spatial distance of exciton delocalization, thereby governing optical responses in molecular aggregates such as superradiance and exciton transport. Notably, biological optoelectronic molecular systems like the FMO complex integrate molecular aggregates characterized by extended ECL, thereby augmenting optical responses.[92−94] Understanding the evolution of ECL is paramount for elucidating energy transfer principles comprehensively. There are many different ways to define ECL,[18,94] to accurately gauge the energy transfer properties of the entire system and reflect essential coherence characteristics among different sites, we present the definition below:[92]

$$L_\rho = \frac{\left(\sum_{ij} |\rho_{ij}|\right)^2}{8 \sum_{ij} |\rho_{ij}|^2}, \qquad 1 \leq L_\rho \leq 8 \tag{27}$$

We first calculate the reduced density matrices of all 8 sites at 0 K, then plot the time evolution of ECL and coherence between different sites in Figure 6. In Figure 6(a), when site 1 is set to be the initial excited position, the ECL goes up in oscillation and reaches the maximum of 2.52 at 443 fs, then it decreases and finally becomes 1.08 at 1000 fs. The reason for this tendency can be obtained from Figure 6(b) to some degree: before about 450 fs, ρ_{12} shows strong fluctuation, while the coherence between other sites also fluctuates in a smaller

range, and their overall trend is upward. Then all coherence between every two sites goes down. These results show consistency to previous findings in the seven-site model, indicating that while site 1 is initially excited, site 8 influences the exciton transport process slightly.[69] Then we discuss the situation when site 8 is initially excited. In Figure 6(c) ECL keeps growing until it reaches a maximum of 2.42 at 692 fs, then turns down and reaches 2.03 at 1000 fs. It shows a smaller amplitude of oscillation overall than ECL in (a). In Figure 6(d), the evolution can be divided into two stages. The first stage is about before 200 fs, during this period ρ_{18} and ρ_{28} first rise and then fall rapidly, and ρ_{12} have a similar trend but a small amplitude. This is because when site 8 is the initial excitation location, as the energy transfer starts, it first passes the exciton to the nearest sites 1 and 2, which leads to a rapid rise and fall of coherence, and there is also exciton transfer between sites 1 and 2 at the closest position, but there is a lag and weakness compared to the transmission of site 8 to 1 and 2. After 200 fs, there comes the second stage. The downward trend of ρ_{12} changes and it keeps increasing until 818 fs, then it begins to go down. It is worth mentioning that, no matter which site is initially excited, the strong interaction between sites 1 and 2 shows a dominant contribution to the total ECL most of the time. ρ_{18} and ρ_{28} shows its importance before 200 fs, while ρ_{38} is always near 0 because of the large distance between sites 8 and 3. ρ_{13} and ρ_{23} stays at a small but steady value, which shows the usage of site 3 to structurally transport exciton to the reaction center.

Then the time-dependent evolution of population dynamics in the eight-site model of the FMO complex, calculated using the TD-DMRG method, is depicted in Figure 7. The simulations start with site 1 (a and b) and site 8 (c and d)
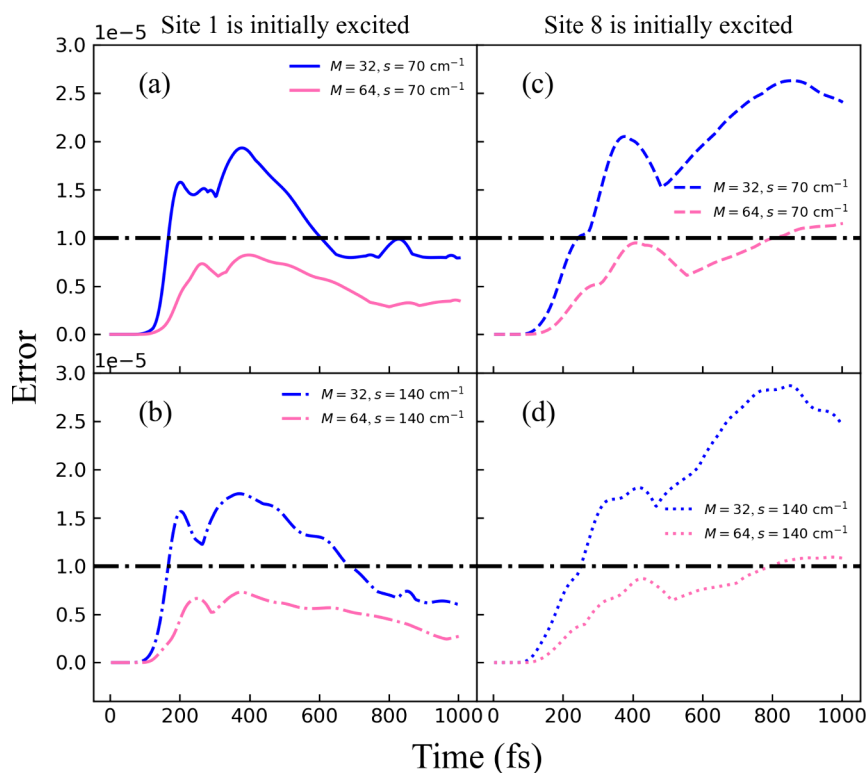
Figure 8. Mean cumulative deviation as a function of evolution time t of different static disorder, different maximum bond dimension M with the result of $M = 128$ to $t = 1000$ fs when site 1 (a and b) or 8 (c and d) is initially excited. Static disorder $s = 70$ cm^{-1} (a and c) or $s = 140$ cm^{-1} (b and d). The temperature is 300 K.

as the initial excitation site, respectively. Figure 7(a) and (c) illustrate the scenario at 0 K, while a comparative analysis is conducted at 300 K using the TFD method mentioned before in Figure 7(b) and (d). The maximum bond dimension M was set to be 128. Remarkably, at 0 K, oscillations can be observed in population dynamics in both Figure 7(a) and (c), albeit more slightly in (c). Upon considering the thermal effects at 300 K, the oscillations are significantly dampened in Figure 7(b) and (d), retaining only small oscillations between sites 1 and 2 when site 8 is initially excited. This phenomenon can be attributed to the thermal effects and the specific initial conditions at sites 1 and 2. Notably, in Figure 6, it seems that the coherence while the initial excitation is at site 8 is comparable or even a bit larger compared to site 1 initial excitation, but in Figure 7(c) there is scarcely any beating. The reason is that the substantial energy gap between site 8 and the other sites, coupled with relatively weak interactions, results in a gradual and incoherent relaxation of population dynamics at site 8, as evident in Figure 7(b). Consequently, the initial conditions at sites 1 and 2 manifest an incoherent distribution, leading to dephasing effects exacerbated by both the temperature and system characteristics, dampening the typical oscillatory behavior. The population at sites 5, 6, and 7 is consistently less than 10%, revealing the dominance of path A in the two energy transfer paths, either with site 1 or 8 as the initial excitation site. Consistent with prior research, our simulations at 300 K align closely with previous findings, corroborating the fidelity of our results.[16]

3.3. The Effect of Static Disorder. Next, the cases including static disorder are considered. The full width at half-maximum (fwhm) of the site energy shift corresponding to the static disorder of each site measured on the FMO trimer has

been given by Chaillet et al.[46] As mentioned earlier, the static disorder is assumed to be in the form of a Gaussian distribution, which allows us to calculate the size of the static disorder from $s = \frac{\text{FWHM}}{2\sqrt{2\ln 2}}$. The results on the first monomer are represented here from site 1 to site 8, which are referred to as the realistic static disorder strength: $s = [36.9, 45.4, 54.6, 39.5, 36.5, 64.3, 50.4, 92.4]$ cm^{-1}. In order to better analyze the influence of the existence of static disorder on the transport process, we first assume that there is a static disorder of the same magnitude in all 8 sites, and all of them only produce a coupling $V = 1$ with their corresponding electronic states. The width of the static disorder distribution varies widely in different sites, while values of around 80 cm^{-1} have been used to fit several experimental results.[95] Considering the above values, we selected $s = 70$ cm^{-1} and $s = 140$ cm^{-1} for analysis to show the effect of static disorder more obviously at first, then we studied the more realistic values. After the addition of static disorder, it is vital to ensure the results of the previous analysis on convergence are still applicable. Different M were considered again and the mean cumulative deviations were calculated. As can be seen in Figure 8, the convergence of the results with respect to M does not change significantly concerning the addition of a static disorder for different initial excitation sites. For the vast majority of the time, the error corresponding to 64 is still below 10^{-5}, which suggests that the results of $M = 128$ are still credible. Moreover, in Figure 8(a) and (c), with the same M, (c) has a larger static disorder and an overall smaller error; However, in Figure 8(b) and (d), at $M = 32$, the static disorder in (d) is larger, but the error is larger generally. Therefore, it can be inferred that there is no clear qualitative relationship between the magnitude of static disorder and the effect of it on convergence.
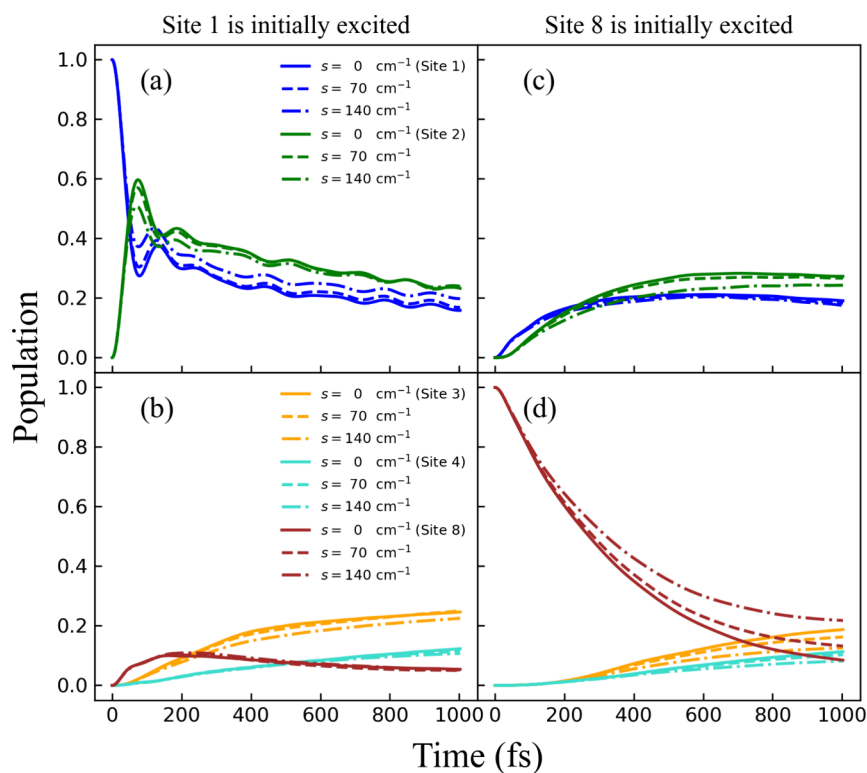
Figure 9. Site populations in the eight-site model of FMO calculated with the TD-DMRG when Bchl 1 (a, b) or 8 (c, d) is initially excited. The populations of sites 5, 6, and 7 are not shown. In all cases, the maximum bond dimension is $M = 128$. The results corresponding to different static disorders $s = 0$, 70, and 140 cm^{-1} are shown in solid, dashed, and dash-dotted lines, respectively. The temperature is 300 K.

Figure 10. Site populations in the eight-site model of FMO calculated with the TD-DMRG when Bchl 1 (a, b) or 8 (c, d) is initially excited. The populations of sites 5, 6, and 7 are not shown. In all cases, the maximum bond dimension is $M = 128$. The results corresponding to none static disorder and realistic static disorders $s = [36.9, 45.4, 54.6, 39.5, 36.5, 64.3, 50.4, 92.4]$ cm^{-1} in site 1 to 8 are shown in solid and dashed lines, respectively. The temperature is 0 K.
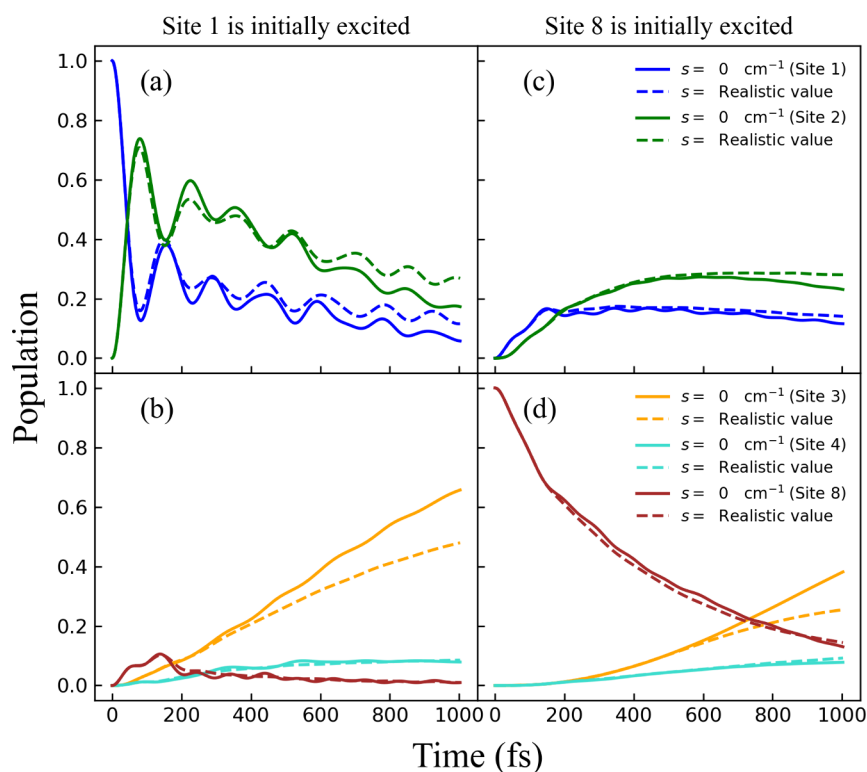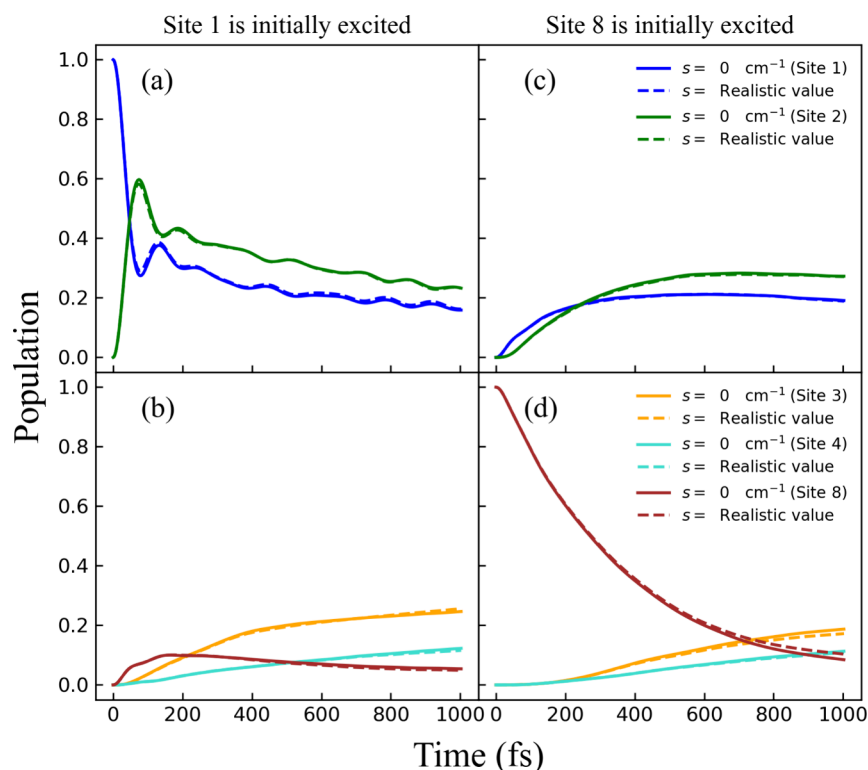
Figure 11. Site populations in the eight-site model of FMO calculated with the TD-DMRG when Bchl 1 (a, b) or 8 (c, d) is initially excited. The populations of sites 5, 6, and 7 are not shown. In all cases, the maximum bond dimension is $M = 128$. The results corresponding to none static disorder and realistic static disorders $s = [36.9, 45.4, 54.6, 39.5, 36.5, 64.3, 50.4, 92.4]$ cm^{-1} in site 1 to 8 are shown in solid and dashed lines, respectively. The temperature is 300 K.

The analysis of site populations with different static disorders is performed. The site population evolution after the addition of static disorder of different sizes is shown in Figure 9. These panels displayed $P_i(t)$ ($i = 1, 2, 3, 4, 8$) without static disorder ($s = 0$, solid lines), with relatively small static disorder ($s = 70$ cm^{-1}, dashed lines) and with relatively strong static disorder ($s = 140$ cm^{-1}, dash-dotted lines) at $T = 300$ K. In Figure 9(a) and (b), while the initial excitation is at site 1, as the static disorder increases, the amplitude of the oscillation of the population on sites 1 and 2 decreases. Also, we observe a decrease in exciton population on sites 2, 3, 4, and 8 during most of the time, whereas site 1 exhibits the opposite trend. A similar situation is shown in Figure 9 (c) and (d): as the static disorder increases, the population on site 8 increases at the same moment as it is the starting excitation site, while population on other sites decreases.

This phenomenon signifies that during the energy transfer process, static disorder diminishes the efficiency of exciton transportation to a certain degree, with the extent of reduction contingent upon the magnitude of static disorder. However, the total trend of population evolution on each site is not affected by static disorder, which means that the entire energy transfer process does not undergo particularly serious changes, such as changes in energy transfer paths. It is also worth mentioning that while site 8 is initially excited, the same static disorder has a more significant impact on it than on other sites. This is because the dwindling exciton population on site 8 is mainly transported to sites 1 and 2 during the energy transfer, as has been analyzed in Sec. 3.2. As the static disorder increases, ρ_{18} and ρ_{28} decrease most of the time, implying a

decrease in the coherence between site 8 and site 1,2, which in turn indicates a decrease in the exciton transport rate.

Following the preceding analysis, we have developed a foundational comprehension of how varying magnitudes of static disorder influence exciton transport. However, it is imperative to acknowledge that the static disorder magnitude differs across individual sites, with realistic values typically smaller than those previously assumed. Comparing the evolution of site populations in the absence of static disorder with outcomes following the inclusion of realistic static disorders, depicted in Figure 10 and Figure 11 for temperatures of 0 and 300 K, respectively, elucidates these dynamics. These panels exhibit the evolution of $P_i(t)$ ($i = 1, 2, 3, 4, 8$) without static disorder ($s = 0$, solid lines) and scenarios incorporating realistic static disorder ($s =$ realistic value, dashed lines). Notably, as can be seen from Figure 10(a) and (b), when site 1 is initially excited, significant variations occur in the exciton population across sites 1, 2, and 3 due to static disorder, while sites 4 and 8 demonstrate minimal changes. The oscillation amplitudes of populations on sites 1 and 2 diminish, with a discernible increase in population compared to the result without static disorder beyond 300 fs, indicative of cumulative effects over time. Conversely, the population on site 3 diminishes in the presence of static disorder. This underscores the progressive manifestation of static disorder's impact on energy transfer dynamics, with discrepancies becoming more pronounced over time. Akin observations are noted on site 3 in Figure 10(c) and (d), where differences in population primarily accentuate after the incorporation of static disorder; but effects on other sites are relatively subdued. There has been much evidence pointing to that the observed
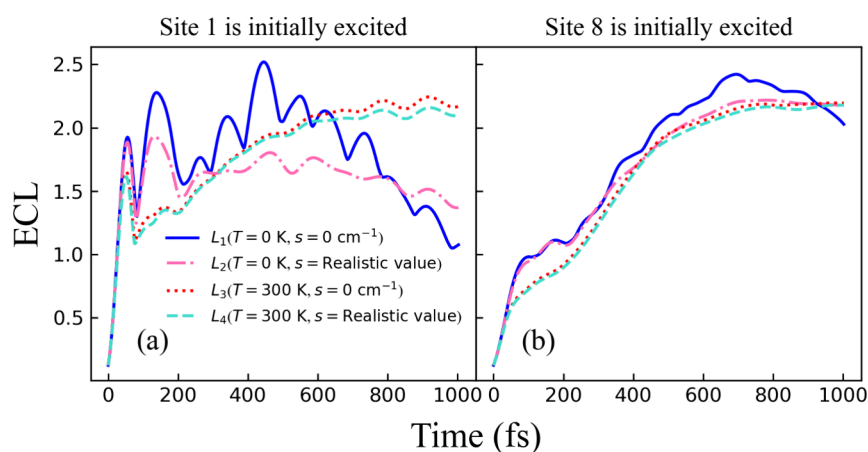
Figure 12. Time evolution of ECLs in the eight-site model of FMO calculated with TD-DMRG when site 1 (a) or 8 (b) is initially excited. The results corresponding to L_1 ($T = 0$ K, $s = 0$), L_2 ($T = 0$ K, s = realistic value), L_3 ($T = 300$ K, $s = 0$) and L_4 ($T = 300$ K, s = realistic value) are shown in solid, dash-dotted, dotted and dashed lines, respectively.

long-lived QBs are inconsistent with interexciton coherence, but a characteristic of Raman-active vibrational modes.[30,96−98] While considering static disorder, some researchers found that electronic coherence vanishes, and only purely vibrational oscillations survive averaging over static disorder after some critical time.[19,99] In Figure 10(a), we noted a similar phenomenon where, after approximately 400 fs, the population oscillation adopts a shape resembling pure vibration. A notable disparity between our findings and those in the study by Gelin et al.[19] lies in the utilization of 74 vibrational modes, potentially accounting for the seemingly increased dephasing in our results. Furthermore, the discrepancy in the number of modes impedes our ability to align our data precisely with vibrations of specific frequencies and hinders the detection of revivals resulting from fortuitous resonances among vibrational frequencies.

However, when we also take the temperature effect into account, the effect of static disorder becomes very limited at 300 K (Figure 11). In order to analyze the effects of temperature and static disorder more quantitatively, we calculated the ECLs for each of the four cases and plotted them in Figure 12. When we focus on the case of $T = 0$ K, it could be found that before 300 fs, the changes in ECLs maintained a similar trend before and after the addition of static disorder (especially when site 8 was initially excited, the two lines were almost overlapped), and only after that began to produce significant differences, which is also consistent with the analysis above: the effects of static disorder gradually appeared after a certain period of accumulation. In Figure 12(a), we get $L_1 = 1.09$ and $L_2 = 1.37$ at 1000 fs, shows a difference of $(L_2 − L_1)/L_1 = 25.7\%$; In Figure 12(b), $L_1 = 2.03$ and $L_2 = 2.18$ at 1000 fs, shows a smaller difference of 7.4%. However, after the temperature effect is considered, the ECLs perform some different phenomena: with the same strength of static disorder, L_3 (L_4) has a great difference compared with L_1 (L_2) since 60 fs, but L_3 is almost coincident with L_4, whatever site is initially excited. In Figure 12(a), L_3 and L_4 has a tiny difference of 3.3% at 1000 fs, while in Figure 12(b) the difference is 0.7% at the end of time evolution. This shows that at a room temperature of 300 K, the static disorder of the realistic strength has little effect on the exciton transport process. The above results indicate that the thermal effect is more dominant than the static disorder effect in influencing energy transfer.

4. CONCLUSION AND OUTLOOK

We explore the exciton dynamics in the FMO complex under static disorder at finite temperatures using the numerically exact TD-DMRG method within a large-site MPS framework. To simulate the finite temperature effects on exciton dynamics, we integrate the thermo-field dynamics and introduce auxiliary bosonic modes to model Gaussian-type static disorders.[70] Our approach combines all electronic degrees of freedom into a single MPS site, a configuration that achieves significant improvements in accuracy with minimal increase in bond dimensions, offering efficiency comparable to traditional setups in similar computational efforts. We thoroughly investigate how different initial excitation sites and the levels of disorder impact the exciton dynamics and the temporal coherence, providing a comprehensive analysis of these effects.

We begin by investigating the impact of different initially excited Bchl sites on exciton dynamics. Our observations reveal that starting from Bchl 8 yields less coherent behavior and diminished efficiency compared to initial excitation from Bchl 1. Likewise, considering a temperature of 300 K instead of 0 K results in a decrease in transport efficiency. Additionally, we analyze the effects of varying strengths of static disorder on the energy transfer process at 300 K, then use realistic static disorder strength to simulate a more realistic situation at both 0 and 300 K. At 0 K, meticulous calculations based on realistic static disorder strengths of each Bchl, typically smaller than $s = 70$ cm^{-1}, indicate a relatively significant influence of static disorder on energy transport. However, when both thermal and static disorders are taken into consideration, our findings suggest that at 300 K, the impact of realistic static disorder becomes negligible. This phenomenon may be elucidated by the notion that at room temperature, the thermal effect outweighs the static disorder effect, inevitably covering the latter's influence.

Our methodology demonstrates potential in precisely studying quantum dynamics across a wide range of exciton−phonon systems. Exploring tensor network structures beyond one-dimensional MPS may further enhance simulation efficiency and scalability.

ASSOCIATED CONTENT

Ⓢ Supporting Information

The Supporting Information is available free of charge at https://pubs.acs.org/doi/10.1021/acs.jctc.4c00493.

Tests on different types of excitation and some complements of the error analysis while comparing different MPS configurations (PDF)

AUTHOR INFORMATION

Corresponding Authors

Weitang Li − *School of Science and Engineering, The Chinese University of Hong Kong, Shenzhen 518172, P. R. China;* ⓞ orcid.org/0000-0002-8739-641X; Email: liwt31@gmail.com

Zhigang Shuai − *School of Science and Engineering, The Chinese University of Hong Kong, Shenzhen 518172, P. R. China; MOE Key Laboratory of Organic OptoElectronics and Molecular Engineering, Department of Chemistry, Tsinghua University, 100084 Beijing, P. R. China;* ⓞ orcid.org/0000-0003-3867-2331; Email: shuaizhigang@cuhk.edu.cn

Authors

Zirui Sheng − *School of Science and Engineering, The Chinese University of Hong Kong, Shenzhen 518172, P. R. China*

Tong Jiang − *MOE Key Laboratory of Organic OptoElectronics and Molecular Engineering, Department of Chemistry, Tsinghua University, 100084 Beijing, P. R. China;* Present Address: Department of Chemistry and Chemical Biology, Harvard University, Cambridge, MA, 02138, USA; ⓞ orcid.org/0000-0002-5907-4886

Complete contact information is available at:
https://pubs.acs.org/10.1021/acs.jctc.4c00493

Notes

The authors declare no competing financial interest.

ACKNOWLEDGMENTS

REFERENCES

(1) Van Amerongen, H.; Van Grondelle, R. *Photosynthetic excitons*; World Scientific, 2000.

(2) Hu, C.-D.; Chinenov, Y.; Kerppola, T. K. Visualization of interactions among bZIP and Rel family proteins in living cells using bimolecular fluorescence complementation. *Mol. Cell* **2002**, *9*, 789−798.

(3) Cogdell, R. J.; Gall, A.; Köhler, J. The architecture and function of the light-harvesting apparatus of purple bacteria: from single molecules to in vivo membranes. *Q. Rev. Biophys.* **2006**, *39*, 227−324.

(4) Jang, S. J.; Mennucci, B. Delocalized excitons in natural light-harvesting complexes. *Rev. Mod. Phys.* **2018**, *90*, 035003.

(5) Blankenship, R. E. *Molecular mechanisms of photosynthesis*; John Wiley & Sons, 2021.

(6) Fenna, R.; Matthews, B. Chlorophyll arrangement in a bacteriochlorophyll protein from Chlorobium limicola. *Nature* **1975**, *258*, 573−577.

(7) Fenna, R.; Ten Eyck, L.; Matthews, B. Atomic coordinates for the chlorophyll core of a bacteriochlorophyll a-protein from green photosynthetic bacteria. *Biochem. Biophys. Res. Commun.* **1977**, *75*, 751−756.

(8) Engel, G. S. Quantum coherence in photosynthesis. *Procedia. Chem.* **2011**, *3*, 222−231.

(9) Ben-Shem, A.; Frolow, F.; Nelson, N. Evolution of photosystem I−from symmetry through pseudosymmetry to asymmetry. *FEBS Lett.* **2004**, *564*, 274−280.

(10) Tronrud, D. E.; Wen, J.; Gay, L.; Blankenship, R. E. The structural basis for the difference in absorbance spectra for the FMO antenna protein from various green sulfur bacteria. *Photosynth. Res.* **2009**, *100*, 79−87.

(11) Schmidt Am Busch, M. S.; Müh, F.; Madjet, M. E.-A.; Renger, T. The eighth bacteriochlorophyll completes the excitation energy funnel in the FMO protein. *J. Phys. Chem. Lett.* **2011**, *2*, 93−98.

(12) Ishizaki, A.; Fleming, G. R. Unified treatment of quantum coherent and incoherent hopping dynamics in electronic energy transfer: Reduced hierarchy equation approach. *J. Chem. Phys.* **2009**, *130*, 234111.

(13) Huo, P.; Coker, D. F. Iterative linearized density matrix propagation for modeling coherent excitation energy transfer in photosynthetic light harvesting. *J. Chem. Phys.* **2010**, *133*, 184108.

(14) Tao, G.; Miller, W. H. Semiclassical description of electronic excitation population transfer in a model photosynthetic system. *J. Phys. Chem. Lett.* **2010**, *1*, 891−894.

(15) Wu, J.; Liu, F.; Ma, J.; Silbey, R. J.; Cao, J. Efficient energy transfer in light-harvesting systems: Quantum-classical comparison, flux network, and robustness analysis. *J. Chem. Phys.* **2012**, *137*, 174111.

(16) Moix, J.; Wu, J.; Huo, P.; Coker, D.; Cao, J. Efficient energy transfer in light-harvesting systems, III: The influence of the eighth bacteriochlorophyll on the dynamics and efficiency in FMO. *J. Phys. Chem. Lett.* **2011**, *2*, 3045−3052.

(17) Hestand, N. J.; Spano, F. C. Expanded theory of H-and J-molecular aggregates: the effects of vibronic coupling and intermolecular charge transfer. *Chem. Rev.* **2018**, *118*, 7069−7163.

(18) Moix, J. M.; Zhao, Y.; Cao, J. Equilibrium-reduced density matrix formulation: Influence of noise, disorder, and temperature on localization in excitonic systems. *Phys. Rev. B* **2012**, *85*, 115412.

(19) Gelin, M. F.; Borrelli, R.; Domcke, W. Origin of unexpectedly simple oscillatory responses in the excited-state dynamics of disordered molecular aggregates. *J. Phys. Chem. Lett.* **2019**, *10*, 2806−2810.

(20) Anderson, P. W. Absence of diffusion in certain random lattices. *Phys. Rev.* **1958**, *109*, 1492.

(21) Scher, H.; Lax, M. Stochastic transport in a disordered solid. I. Theory. *Phys. Rev. B* **1973**, *7*, 4491.

(22) Schein, L.; Glatz, D.; Scott, J. Observation of the transition from adiabatic to nonadiabatic small polaron hopping in a molecularly doped polymer. *Phys. Rev. Lett.* **1990**, *65*, 472.

(23) Kenkre, V.; Dunlap, D. Charge transport in molecular solids: dynamic and static disorder. *Philos. Mag. B* **1992**, *65*, 831−841.

(24) Parris, P. E.; Kenkre, V. M.; Dunlap, D. H. Nature of charge carriers in disordered molecular solids: Are polarons compatible with observations? *Phys. Rev. Lett.* **2001**, *87*, 126601.

(25) Tempelaar, R.; Jansen, T. L.; Knoester, J. Vibrational beatings conceal evidence of electronic coherence in the FMO light-harvesting complex. *J. Phys. Chem. B* **2014**, *118*, 12865−12872.

(26) Butkus, V.; Zigmantas, D.; Valkunas, L.; Abramavicius, D. Vibrational vs. electronic coherences in 2D spectrum of molecular systems. *Chem. Phys. Lett.* **2012**, *545*, 40−43.

(27) Duan, H.-G.; Nalbach, P.; Prokhorenko, V. I.; Mukamel, S.; Thorwart, M. On the origin of oscillations in two-dimensional spectra of excitonically-coupled molecular systems. *New J. Phys.* **2015**, *17*, 072002.

(28) Halpin, A.; Johnson, P. J.; Tempelaar, R.; Murphy, R. S.; Knoester, J.; Jansen, T. L.; Miller, R. D. Two-dimensional spectros-

copy of a molecular dimer unveils the effects of vibronic coupling on exciton coherences. *Nat. Chem.* **2014**, *6*, 196−201.

(29) Lambert, N.; Chen, Y.-N.; Cheng, Y.-C.; Li, C.-M.; Chen, G.-Y.; Nori, F. Quantum biology. *Nat. Phys.* **2013**, *9*, 10−18.

(30) Cao, J.; Cogdell, R. J.; Coker, D. F.; Duan, H.-G.; Hauer, J.; Kleinekathöfer, U.; Jansen, T. L.; Mančal, T.; Miller, R. D.; Ogilvie, J. P.; et al. Quantum biology revisited. *Sci. Adv.* **2020**, *6*, No. eaaz4888.

(31) Pullerits, T.; Chachisvilis, M.; Sundström, V. Exciton delocalization length in the B850 antenna of Rhodobacter sphaeroides. *J. Phys. Chem.* **1996**, *100*, 10787−10792.

(32) Monshouwer, R.; Abrahamsson, M.; van Mourik, F.; van Grondelle, R. Superradiance and exciton delocalization in bacterial photosynthetic light-harvesting systems. *J. Phys. Chem. B* **1997**, *101*, 7241−7248.

(33) Mukamel, S. *Principles of nonlinear optical spectroscopy*; 1995.

(34) Saito, S.; Higashi, M.; Fleming, G. R. Site-dependent fluctuations optimize electronic energy transfer in the Fenna−Matthews−Olson protein. *J. Phys. Chem. B* **2019**, *123*, 9762−9772.

(35) Olbrich, C.; Strumpfer, J.; Schulten, K.; Kleinekathofer, U. Theory and simulation of the environmental effects on FMO electronic transitions. *J. Phys. Chem. Lett.* **2011**, *2*, 1771−1776.

(36) Rivera, E.; Montemayor, D.; Masia, M.; Coker, D. F. Influence of site-dependent pigment−protein interactions on excitation energy transfer in photosynthetic light harvesting. *J. Phys. Chem. B* **2013**, *117*, 5510−5521.

(37) Chandrasekaran, S.; Aghtar, M.; Valleau, S.; Aspuru-Guzik, A.; Kleinekathöfer, U. Influence of force fields and quantum chemistry approach on spectral densities of BChl a in solution and in FMO proteins. *J. Phys. Chem. B* **2015**, *119*, 9995−10004.

(38) Lee, M. K.; Coker, D. F. Modeling electronic-nuclear interactions for excitation energy transfer processes in light-harvesting complexes. *J. Phys. Chem. Lett.* **2016**, *7*, 3171−3178.

(39) Kim, C. W.; Rhee, Y. M. Constructing an interpolated potential energy surface of a large molecule: A case study with bacterio-chlorophyll a model in the Fenna−Matthews−Olson complex. *J. Chem. Theory Comput.* **2016**, *12*, 5235−5246.

(40) Kim, C. W.; Choi, B.; Rhee, Y. M. Excited state energy fluctuations in the Fenna−Matthews−Olson complex from molecular dynamics simulations with interpolated chromophore potentials. *Phys. Chem. Chem. Phys.* **2018**, *20*, 3310−3319.

(41) Rosnik, A. M.; Curutchet, C. Theoretical characterization of the spectral density of the water-soluble chlorophyll-binding protein from combined quantum mechanics/molecular mechanics molecular dynamics simulations. *J. Chem. Theory Comput.* **2015**, *11*, 5826−5837.

(42) Blau, S. M.; Bennett, D. I.; Kreisbeck, C.; Scholes, G. D.; Aspuru-Guzik, A. Local protein solvation drives direct down-conversion in phycobiliprotein PC645 via incoherent vibronic transport. *Proc. Natl. Acad. Sci. U. S. A.* **2018**, *115*, E3342−E3350.

(43) Maity, S.; Bold, B. M.; Prajapati, J. D.; Sokolov, M.; Kubar, T.; Elstner, M.; Kleinekathöfer, U. DFTB/MM molecular dynamics simulations of the FMO light-harvesting complex. *J. Phys. Chem. Lett.* **2020**, *11*, 8660−8667.

(44) Wells, S.; Menor, S.; Hespenheide, B.; Thorpe, M. F. Constrained geometric simulation of diffusive motion in proteins. *Phys. Biol.* **2005**, *2*, S127.

(45) Adolphs, J.; Müh, F.; Madjet, M. E.-A.; Renger, T. Calculation of pigment transition energies in the FMO protein: From simplicity to complexity and back. *Photosynth. Res.* **2008**, *95*, 197−209.

(46) Chaillet, M. L.; Lengauer, F.; Adolphs, J.; Müh, F.; Fokas, A. S.; Cole, D. J.; Chin, A. W.; Renger, T. Static disorder in excitation energies of the Fenna−Matthews−Olson protein: Structure-based theory meets experiment. *J. Phys. Chem. Lett.* **2020**, *11*, 10306−10314.

(47) Brédas, J.-L.; Sargent, E. H.; Scholes, G. D. Photovoltaic concepts inspired by coherence effects in photosynthetic systems. *Nat. Mater.* **2017**, *16*, 35−44.

(48) Yan, J.; Rezasoltani, E.; Azzouzi, M.; Eisner, F.; Nelson, J. Influence of static disorder of charge transfer state on voltage loss in organic photovoltaics. *Nat. Commun.* **2021**, *12*, 3642.

(49) Yu, S.; Qiu, C.-W.; Chong, Y.; Torquato, S.; Park, N. Engineered disorder in photonics. *Nat. Rev. Mater.* **2021**, *6*, 226−243.

(50) Ren, J.; Shuai, Z.; Kin-Lic Chan, G. Time-dependent density matrix renormalization group algorithms for nearly exact absorption and fluorescence spectra of molecular aggregates at both zero and finite temperature. *J. Chem. Theory Comput.* **2018**, *14*, 5027−5039.

(51) Baiardi, A.; Reiher, M. Large-scale quantum dynamics with matrix product states. *J. Chem. Theory Comput.* **2019**, *15*, 3481−3498.

(52) Jiang, T.; Li, W.; Ren, J.; Shuai, Z. Finite temperature dynamical density matrix renormalization group for spectroscopy in frequency domain. *J. Phys. Chem. Lett.* **2020**, *11*, 3761−3768.

(53) Jiang, T.; Ren, J.; Shuai, Z. Chebyshev matrix product states with canonical orthogonalization for spectral functions of many-body systems. *J. Phys. Chem. Lett.* **2021**, *12*, 9344−9352.

(54) Yao, Y.; Xie, X.; Ma, H. Ultrafast long-range charge separation in organic photovoltaics: promotion by off-diagonal vibronic couplings and entropy increase. *J. Phys. Chem. Lett.* **2016**, *7*, 4830−4835.

(55) Greene, S. M.; Batista, V. S. Tensor-train split-operator fourier transform (TT-SOFT) method: Multidimensional nonadiabatic quantum dynamics. *J. Chem. Theory Comput.* **2017**, *13*, 4034−4042.

(56) Ren, J.; Li, W.; Jiang, T.; Wang, Y.; Shuai, Z. Time-dependent density matrix renormalization group method for quantum dynamics in complex systems. *Wiley Interdiscip. Rev. Comput. Mol. Sci.* **2022**, *12*, No. e1614.

(57) Wang, Y.; Ren, J.; Shuai, Z. Evaluating the anharmonicity contributions to the molecular excited state internal conversion rates with finite temperature TD-DMRG. *J. Chem. Phys.* **2021**, *154*, 214109.

(58) Wang, Y.; Ren, J.; Shuai, Z. Minimizing non-radiative decay in molecular aggregates through control of excitonic coupling. *Nat. Commun.* **2023**, *14*, 5056.

(59) Yang, H.; Li, W.; Ren, J.; Shuai, Z. Time-Dependent Density Matrix Renormalization Group Method for Quantum Transport with Phonon Coupling in Molecular Junction. *J. Chem. Theory Comput.* **2023**, *19*, 6070−6081.

(60) Li, W.; Ren, J.; Shuai, Z. A general charge transport picture for organic semiconductors with nonlocal electron-phonon couplings. *Nat. Commun.* **2021**, *12*, 4260.

(61) Ge, Y.; Li, W.; Ren, J.; Shuai, Z. Computational method for evaluating the thermoelectric power factor for organic materials modeled by the Holstein model: A time-dependent density matrix renormalization group formalism. *J. Chem. Theory Comput.* **2022**, *18*, 6437−6446.

(62) Meyer, H.-D.; Manthe, U.; Cederbaum, L. S. The multi-configurational time-dependent Hartree approach. *Chem. Phys. Lett.* **1990**, *165*, 73−78.

(63) Manthe, U. The multi-configurational time-dependent Hartree approach revisited. *J. Chem. Phys.* **2015**, *142*, 4922889.

(64) Wang, H.; Thoss, M. Multilayer formulation of the multi-configuration time-dependent Hartree theory. *J. Chem. Phys.* **2003**, *119*, 1289−1299.

(65) Haegeman, J.; Cirac, J. I.; Osborne, T. J.; Pižorn, I.; Verschelde, H.; Verstraete, F. Time-dependent variational principle for quantum lattices. *Phys. Rev. Lett.* **2011**, *107*, 070601.

(66) Chin, A. W.; Prior, J.; Rosenbach, R.; Caycedo-Soler, F.; Huelga, S. F.; Plenio, M. B. The role of non-equilibrium vibrational structures in electronic coherence and recoherence in pigment−protein complexes. *Nat. Phys.* **2013**, *9*, 113−118.

(67) Borrelli, R.; Gelin, M. F. Simulation of quantum dynamics of excitonic systems at finite temperature: An efficient method based on thermo field dynamics. *Sci. Rep.* **2017**, *7*, 9127.

(68) Li, W.; Ren, J.; Shuai, Z. Numerical assessment for accuracy and GPU acceleration of TD-DMRG time evolution schemes. *J. Chem. Phys.* **2020**, *152*, 024127.

(69) Schulze, J.; Shibl, M. F.; Al-Marri, M. J.; Kühn, O. Multi-layer multi-configuration time-dependent Hartree (ML-MCTDH) approach to the correlated exciton-vibrational dynamics in the FMO complex. *J. Chem. Phys.* **2016**, *144*, 185101.

(70) Gelin, M. F.; Velardo, A.; Borrelli, R. Efficient quantum dynamics simulations of complex molecular systems: A unified treatment of dynamic and static disorder. *J. Chem. Phys.* **2021**, *155*, 134102.

(71) Borrelli, R.; Gelin, M. F. Quantum electron-vibrational dynamics at finite temperature: Thermo field dynamics approach. *J. Chem. Phys.* **2016**, *145*, 224101.

(72) Nelson, T. R.; Ondarse-Alvarez, D.; Oldani, N.; Rodriguez-Hernandez, B.; Alfonso-Hernandez, L.; Galindo, J. F.; Kleiman, V. D.; Fernandez-Alberti, S.; Roitberg, A. E.; Tretiak, S. Coherent exciton-vibrational dynamics and energy transfer in conjugated organics. *Nat. Commun.* **2018**, *9*, 2316.

(73) Schröter, M.; Ivanov, S. D.; Schulze, J.; Polyutov, S. P.; Yan, Y.; Pullerits, T.; Kühn, O. Exciton−vibrational coupling in the dynamics and spectroscopy of Frenkel excitons in molecular aggregates. *Phys. Rep.* **2015**, *567*, 1−78.

(74) Matsumoto, H.; Nakano, Y.; Umezawa, H.; Mancini, F.; Marinaro, M. Thermo field dynamics in interaction representation. *Prog. Theor. Phys.* **1983**, *70*, 599−602.

(75) Semenoff, G. W.; Umezawa, H. Functional methods in thermofield dynamics: A real-time perturbation theory for quantum statistical mechanics. *Nucl. Phys. B* **1983**, *220*, 196−212.

(76) Umezawa, H. Methods of Quantum Field Theory in Condensed Matter Physics: —New Perspectives, Extensions and Applications. *Progr. Theor. Phys. Suppl.* **1984**, *80*, 26−39.

(77) Evans, T.; Hardman, I.; Umezawa, H.; Yamanaka, Y. Heisenberg and interaction representations in thermo field dynamics. *jmp* **1992**, *33*, 370−378.

(78) Paeckel, S.; Köhler, T.; Swoboda, A.; Manmana, S. R.; Schollwöck, U.; Hubig, C. Time-evolution methods for matrix-product states. *Ann. Phys.* **2019**, *411*, 167998.

(79) Schollwöck, U. The density-matrix renormalization group in the age of matrix product states. *Ann. Phys.* **2011**, *326*, 96−192.

(80) White, S. R.; Martin, R. L. Ab initio quantum chemistry using the density matrix renormalization group. *J. Chem. Phys.* **1999**, *110*, 4127−4130.

(81) Larsson, H. R.; Zhai, H.; Gunst, K.; Chan, G. K.-L. Matrix product states with large sites. *J. Chem. Theory Comput.* **2022**, *18*, 749−762.

(82) Wendling, M.; Pullerits, T.; Przyjalgowski, M. A.; Vulto, S. I.; Aartsma, T. J.; van Grondelle, R.; van Amerongen, H. Electron-Vibrational Coupling in the Fenna- Matthews- Olson Complex of Prosthecochloris a estuarii Determined by Temperature-Dependent Absorption and Fluorescence Line-Narrowing Measurements. *J. Phys. Chem. B* **2000**, *104*, 5825−5831.

(83) García-Ripoll, J. J. Time evolution of matrix product states. *New J. Phys.* **2006**, *8*, 305.

(84) Dirac, P. A. Note on exchange phenomena in the Thomas atom. *Mathematical proceedings of the Cambridge philosophical society* **1930**, *26*, 376−385.

(85) Gatti, F.; Lasorne, B.; Meyer, H.-D.; Nauts, A. *Applications of quantum dynamics in chemistry*; Springer, 2017; Vol. *98*.

(86) Moritz, G.; Hess, B. A.; Reiher, M. Convergence behavior of the density-matrix renormalization group algorithm for optimized orbital orderings. *J. Chem. Phys.* **2005**, *122*, 024107.

(87) Olivares-Amaya, R.; Hu, W.; Nakatani, N.; Sharma, S.; Yang, J.; Chan, G. K. The ab-initio density matrix renormalization group in practice. *J. Chem. Phys.* **2015**, *142*, 034102.

(88) Xie, X.; Liu, Y.; Yao, Y.; Schollwöck, U.; Liu, C.; Ma, H. Time-dependent density matrix renormalization group quantum dynamics for realistic chemical systems. *J. Chem. Phys.* **2019**, *151*, 224101.

(89) Li, W.; Ren, J.; Yang, H.; Shuai, Z. On the fly swapping algorithm for ordering of degrees of freedom in density matrix renormalization group. *J. Phys.: Condens. Matter* **2022**, *34*, 254003.

(90) Ishizaki, A.; Fleming, G. R. Theoretical examination of quantum coherence in a photosynthetic system at physiological temperature. *Proc. Natl. Acad. Sci. U. S. A.* **2009**, *106*, 17255−17260.

(91) Ullah, A.; Dral, P. O. Predicting the future of excitation energy transfer in light-harvesting complex with artificial intelligence-based quantum dynamics. *Nat. Commun.* **2022**, *13*, 1930.

(92) Meier, T.; Zhao, Y.; Chernyak, V.; Mukamel, S. Polarons, localization, and excitonic coherence in superradiance of biological antenna complexes. *J. Chem. Phys.* **1997**, *107*, 3876−3893.

(93) Scholes, G. D.; Fleming, G. R.; Chen, L. X.; Aspuru-Guzik, A.; Buchleitner, A.; Coker, D. F.; Engel, G. S.; Van Grondelle, R.; Ishizaki, A.; Jonas, D. M.; et al. Using coherence to enhance function in chemical and biophysical systems. *Nature* **2017**, *543*, 647−656.

(94) Jiang, T.; Ren, J.; Shuai, Z. Unified Definition of Exciton Coherence Length for Exciton−Phonon Coupled Molecular Aggregates. *J. Phys. Chem. Lett.* **2023**, *14*, 4541−4547.

(95) Milder, M. T.; Brüggemann, B.; van Grondelle, R.; Herek, J. L. Revisiting the optical properties of the FMO protein. *Photosynth. Res.* **2010**, *104*, 257−274.

(96) Duan, H.-G.; Prokhorenko, V. I.; Cogdell, R. J.; Ashraf, K.; Stevens, A. L.; Thorwart, M.; Miller, R. D. Nature does not rely on long-lived electronic quantum coherence for photosynthetic energy transfer. *Proc. Natl. Acad. Sci. U. S. A.* **2017**, *114*, 8493−8498.

(97) Maiuri, M.; Ostroumov, E. E.; Saer, R. G.; Blankenship, R. E.; Scholes, G. D. Coherent wavepackets in the Fenna−Matthews−Olson complex are robust to excitonic-structure perturbations caused by mutagenesis. *Nat. Chem.* **2018**, *10*, 177−183.

(98) Thyrhaug, E.; Tempelaar, R.; Alcocer, M. J.; Žídek, K.; Bína, D.; Knoester, J.; Jansen, T. L.; Zigmantas, D. Identification and characterization of diverse coherences in the Fenna−Matthews−Olson complex. *Nat. Chem.* **2018**, *10*, 780−786.

(99) Kreisbeck, C.; Kramer, T. Long-lived electronic coherence in dissipative exciton dynamics of light-harvesting complexes. *J. Phys. Chem. Lett.* **2012**, *3*, 2828−2833.